

Ion Imaging via Long-Range Interaction with Rydberg Atoms

Christian Gross,^{1,†} Thibault Vogt^{1,2,†} and Wenhui Li^{1,3,*}

¹Centre for Quantum Technologies, National University of Singapore, 3 Science Drive 2, Singapore 117543

²MajuLab, CNRS-UCA-SU-NUS-NTU International Joint Research Unit, Singapore 117543

³Department of Physics, National University of Singapore, Singapore 117542

 (Received 18 October 2019; accepted 7 January 2020; published 4 February 2020)

We demonstrate imaging of ions in an atomic gas with ion–Rydberg-atom interaction induced absorption. This is made possible by utilizing a multiphoton electromagnetically induced transparency (EIT) scheme and the extremely large electric polarizability of a Rydberg state with high orbital angular momentum. We process the acquired images to obtain the distribution of ion clouds and to spectroscopically investigate the effect of the ions on the EIT resonance. Furthermore, we show that our method can be employed to image the dynamics of ions in a time resolved way. As an example, we map out the avalanche ionization of a gas of Rydberg atoms. The minimal disruption and the flexibility offered by this imaging technique make it ideally suited for the investigation of cold hybrid ion-atom systems.

DOI: [10.1103/PhysRevLett.124.053401](https://doi.org/10.1103/PhysRevLett.124.053401)

The exaggerated polarizability and dipole moment of a highly excited (Rydberg) atom [1] result in its extreme sensitivity to electric fields ranging from static to terahertz regimes, as well as strong interactions with charged particles and other Rydberg atoms. These properties have enabled applications in the research fields of electric field sensing [2–5], quantum optics at the single-photon level [6–9], quantum information processing [10], and quantum simulation of many-body systems [11,12]. Furthermore, the strong interactions between ions and Rydberg atoms are central to the recently observed Rydberg excitation blockade by a single ion [13] and to predictions on the control of cold atom-ion collisions via Rydberg dressing [14,15]. These studies are actively pursued in relation to cold hybrid ion-atom systems, which are emerging as a new platform for investigating fundamental quantum physics, including cold collisions, strong coupling polarons, formation of molecular ions, and charge mobilities [16,17]. The ability to image the ion kinetics *in situ* and nondestructively will be highly relevant for probing such processes.

In this context, electromagnetically induced transparency involving Rydberg states (Rydberg EIT) is promising for imaging the dynamics of ion impurities immersed in cold atom clouds. The underlying idea is to utilize interaction enhanced photon scattering due to the Rydberg excitation blockade [13,18,19]. A similar concept has been implemented to image impurity Rydberg atoms and monitor dipole-mediated energy transport [20,21]. As the imaging technique relies on the absorption of light by a large number of atoms surrounding each ion, it has the potential of being fast and could be applied to ions of any internal structure.

In this Letter, we demonstrate imaging of $^{87}\text{Rb}^+$ ions embedded in a cold cloud of ^{87}Rb atoms with ion–Rydberg-atom interaction induced absorption. We expose the ion-atom mixture to an imaging probe pulse of 1 μs under the conditions of a multiphoton EIT scheme involving the 27G Rydberg state. From the acquired images, we quantitatively analyze the spectral shift and the suppression of the EIT resonance in the presence of ions. Finally, we report a spatially and temporally resolved observation of the avalanche ionization dynamics in a Rydberg gas. This result shows that this imaging technique is well suited to investigate the dynamics of cold hybrid ion-atom systems.

The principle of the imaging method is illustrated in Fig. 1(a). A probe beam resonantly drives the atomic transition from the ground state $|g\rangle$ to an excited state $|e\rangle$ while a coupling field is on resonance with the transition from $|e\rangle$ to a Rydberg state $|r\rangle$. In the vicinity of an ion, the energy level $|r\rangle$ is shifted due to the long-range ion–Rydberg-atom interaction potential $V_{\text{IR}}(R) = -C_4/R^4$, where R is the internuclear distance and C_4 is the interaction coefficient. Inside the so-called blockade sphere of radius $R_b = (2C_4/\gamma_{\text{EIT}})^{1/4}$, this shift exceeds the EIT linewidth γ_{EIT} , which enhances scattering from state $|e\rangle$. Therefore, the atoms within the blockade sphere surrounding an ion absorb the probe light, whereas the rest of the atomic ensemble remains transparent, and this contrast is used to form an image of the ion.

Note that, even in the absence of ions, the transmission of the probe light may be reduced due to the Rydberg–Rydberg interaction $V_{\text{RR}}(R) = -C_6/R^6$ [23,24]. Hence, the critical aspect to achieve a sufficient imaging contrast is to properly select the Rydberg state $|r\rangle$, such that $V_{\text{IR}}(R)$ is strong enough to induce a large absorption around the ion

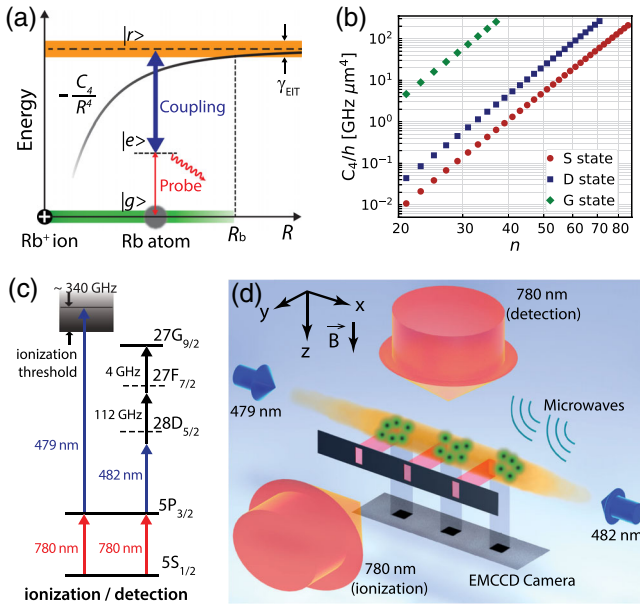


FIG. 1. (a) Concept of the ion–Rydberg-atom interaction induced absorption. (b) Plots of C_4 coefficients of the interaction $V_{\text{IR}}(R)$ between a $^{87}\text{Rb}^+$ ion and a ^{87}Rb Rydberg atom in the $|nG_{9/2}, m_J = 9/2\rangle$ state (green diamonds), the $|nD_{5/2}, m_J = 5/2\rangle$ state (blue squares), and the $|nS_{1/2}, m_J = 1/2\rangle$ state (red dots) [22]. (c) Photoionization and multiphoton Rydberg EIT detection schemes. (d) Sketch of the experimental setup. A bias B field along z defines the quantization axis. The 479 nm ionization beam is aligned along x with the axial axis of the atomic ensemble. The 780 nm ionization beam passes through a pattern of one or more slits, which is imaged onto the atomic cloud using a 1.8:1 relay telescope (not shown). The detection fields include a 780 nm probe laser, a 482 nm laser beam counterpropagating with the 479 nm beam, and two microwave fields with wave vectors in the $x - y$ plane. The probe light is scattered inside the Rydberg blockade spheres (green balls) around the ions (black dots), which cast shadows on an electron-multiplying charge-coupled-device (EMCCD) camera.

while $V_{\text{RR}}(R)$ remains weak. We accomplish this by virtue of the strong dependence of the Rydberg state polarizability $\alpha = 2(4\pi\epsilon_0/e)^2 C_4$ on the orbital angular momentum ℓ of the Rydberg state [22], where ϵ_0 is the electric constant and e is the elementary charge. As shown in Fig. 1(b), the C_4 coefficient for a G state is 2 orders of magnitude larger than those for the S and D states of a similar principal quantum number n , due to its proximity in energy to the neighboring states of opposite parity. This huge C_4 coefficient leads to a blockade radius $R_b > 5 \mu\text{m}$ for a wide range of γ_{EIT} in our experiment and for n as low as $n = 20$. A Rydberg state of low ℓ and high n may have a C_4 coefficient similar to that for a G state of low n , but a C_6 coefficient 3 orders of magnitude larger. This C_6 would result in a nearly complete absorption of the EIT probe light under the experimental conditions necessary for imaging [24]. In balancing the two interaction effects as well as taking into account technical factors in our setup, we have chosen the state

$|r_0\rangle = |27G_{9/2}, m_J = 9/2\rangle$ as the upper EIT level, which we access via a multiphoton EIT scheme [25].

We begin our experiment with the preparation of an ensemble of ^{87}Rb atoms in the ground state $|g\rangle = |5S_{1/2}, F = 2, m_F = 2\rangle$, which is confined in a single-beam optical dipole trap (ODT) at a temperature of $25 \mu\text{K}$. After being released from the ODT and a time-of-flight of $10 \mu\text{s}$, the highly elongated atomic cloud has a peak density of $4.8 \times 10^{11} \text{cm}^{-3}$ and radially follows a Gaussian density distribution with a $1/e^2$ radius $w = 12 \mu\text{m}$. To produce ions, we use the two-photon ionization scheme shown in Fig. 1(c), where a 780 nm laser resonantly drives the transition to the intermediate state $|e\rangle = |5P_{3/2}, F = 3, m_F = 3\rangle$, and a 479 nm laser provides the coupling to the continuum at about $2\pi \times 340 \text{GHz}$ above the ionization threshold. The photoionization lasers are applied for a duration of $t_i = 0.14 \mu\text{s}$ to generate ions within well-defined regions of the atomic ensemble, as illustrated in Fig. 1(d).

Following the two-photon ionization pulse and a delay of $0.1 \mu\text{s}$, we perform imaging with a $1 \mu\text{s}$ EIT detection pulse. As shown in Fig. 1(c), the probe field of wavelength $\lambda_p = 780 \text{nm}$ couples to the $|g\rangle \rightarrow |e\rangle$ atomic transition. An effective three-photon coupling field is used to enable the $|e\rangle \rightarrow |r_0\rangle$ transition via the off-resonant intermediate states $|28D_{5/2}, m_J = 5/2\rangle$ and $|27F_{7/2}, m_J = 7/2\rangle$. It is formed by the optical field D (482 nm) and the two microwave fields $M1$ (112 GHz) and $M2$ (4 GHz). The spatial configuration of the imaging fields is shown in Fig. 1(d). The circularly polarized probe beam of peak Rabi frequency $\Omega_p = 2\pi \times 0.7 \text{MHz}$ propagates through the atomic cloud along the quantization axis z and is projected onto the EMCCD camera using an imaging system of $3 \mu\text{m}$ resolution [26]. We choose a magnetic field B of 6.1 G to induce sufficiently large Zeeman splittings of the energy levels and appropriate frequencies and helicities of the fields D , $M1$, and $M2$, such that only the σ^+ transitions are of relevance in our experiment. These three fields form an effective coupling field, with experimentally calibrated Rabi frequency $\Omega_{\text{C,eff}} = 2\pi \times 6.7 \text{MHz}$. Further experimental details on the imaging fields are given in Ref. [27].

The obtained images are preprocessed to remove undesirable interference fringes [31] and then averaged over many experimental cycles. In the absence of the ionization pulse, we observe an approximately uniform absorption along the atomic cloud under resonant EIT conditions, as shown in Fig. 2(a). This residual absorption is due to the Rydberg blockade induced dissipation resulting from the interaction $V_{\text{RR}}(R)$ [23,24]. It could be reduced by lowering Ω_p , which, however, would be detrimental to the imaging signal-to-noise ratio. When an ionization pulse is applied in three different regions of the atomic cloud, as indicated by dashed lines in Fig. 2(b), an enhanced absorption is observed at the positions of the ion clouds. We extract the image of ions by computing the relative transmission at every pixel position (x, y) ,

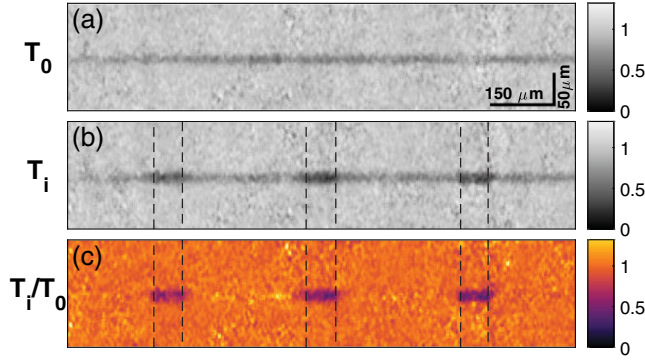


FIG. 2. Imaging of ion clouds. (a) EIT image T_0 acquired without ions. (b) EIT image T_i acquired in the presence of three ion clouds. (c) Image of the relative transmission T_i/T_0 . Each of the images (a) and (b) is the average of about 220 preprocessed images. The dashed lines delimit the areas where the atoms are exposed to the photoionization 780 nm laser beam. About 11 ions are created in each of the three exposed areas.

$$T(x, y) = \frac{T_i(x, y)}{T_0(x, y)}, \quad (1)$$

where T_i and T_0 correspond to the transmission images acquired with and without applied ionization pulse, respectively. This postprocessing highlights the local character of the ion distribution, as shown in Fig. 2(c).

The images of Figs. 2(a) and 2(b) are acquired under optimized conditions based on the spectroscopic studies shown in Fig. 3. For the measurements in Fig. 3, we apply a photoionization pulse in a single region of the atomic cloud and vary the probe field frequency detuning Δ_p at the beginning of each experimental cycle, while keeping all other parameters unchanged. The two four-photon EIT spectra in Fig. 3(a) correspond to the mean transmissions \bar{T}_i and \bar{T}_0 recorded with and without ionization pulse, respectively. Here, \bar{T}_i and \bar{T}_0 are calculated over the small region of interest indicated by a rectangle in the inset image of Fig. 3(a).

In the absence of the ionization pulse, the spectrum is similar to those of standard Rydberg EIT configurations [32], as confirmed by a fit with the steady-state solution of a three-level EIT system [Fig. 3(a)]. We observe a characteristic transmission peak centered in the broad atomic absorption spectrum, which, however, is shifted from the atomic transition frequency by $\Delta_{p0} \approx 2\pi \times 8$ MHz. This shift is due to ac Stark shifts coming from the off-resonant fields that form the effective coupling field [25]. In the presence of the ionization pulse, generating approximately 14 ions, the drop in transmission is sharp around Δ_{p0} . This drop is due to interaction enhanced scattering within the blockade sphere of radius R_b around each impurity ion. Using the ion-atom interaction coefficient for $|r_0\rangle$ given in Fig. 1(a), $C_4/h = 26.5$ GHz μm^4 , we obtain $R_b = 8.5$ μm , which is comparable to the radius of the atomic cloud.

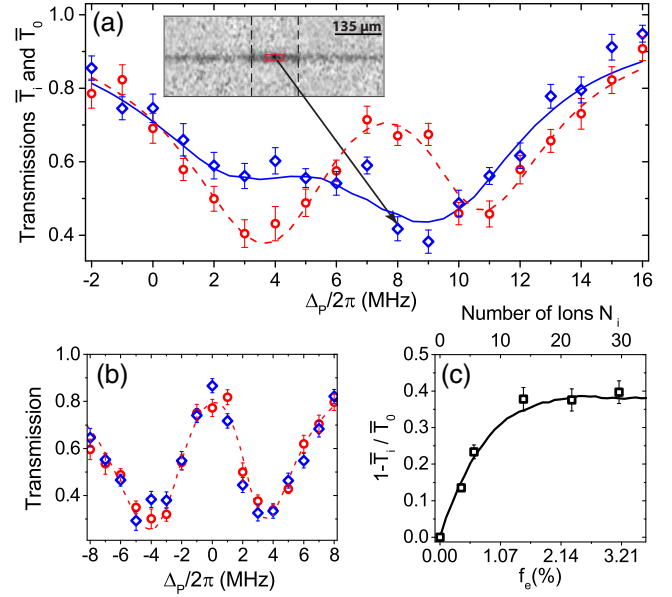


FIG. 3. (a),(b) EIT spectra showing mean probe transmissions \bar{T}_i and \bar{T}_0 vs probe field detuning Δ_p using the Rydberg state $|27G_{9/2}, m_J = 9/2\rangle$ in (a) and $|28D_{5/2}, m_J = 5/2\rangle$ in (b). The data markers correspond to experimental spectra recorded without ions (red circles) and with ions (blue diamonds). The EIT image T_i shown in the inset is the average of 22 preprocessed images. (c) Relative absorption $\mathcal{A} = 1 - \bar{T}_i/\bar{T}_0$ recorded for $\Delta_p = 2\pi \times 8$ MHz as a function of f_e and N_i . The dashed lines are three-level EIT fits, and the solid lines are the result of a theoretical model as detailed in the text. The error bars are the standard error over more than 20 imaging realizations.

This large blockade radius is consistent with the disappearance of the EIT effect at Δ_{p0} . Moreover, the EIT resonance is redshifted by about $2\pi \times 2.5$ MHz from Δ_{p0} , while being broadened and strongly attenuated. This is due to the attractive and inhomogeneous ion–Rydberg-atom interaction in the present system.

The large C_4 coefficient of state $|r_0\rangle$ is essential for this imaging technique. To verify this, we change the upper EIT state from $|r_0\rangle$ to the nearby $|28D_{5/2}, m_J = 5/2\rangle$ state having a C_4 coefficient 2 orders of magnitude smaller. We achieve this with a standard two-photon EIT scheme, where the coupling field is provided by a single 482 nm laser. The corresponding EIT spectra acquired with and without ionization pulse are shown in Fig. 3(b), and no clear difference is noticeable. This is expected, as the blockade radius in this case is reduced threefold, which means that ~ 30 times fewer probe photons are scattered off around an ion.

In Fig. 3(c), we report on the relative absorption $\mathcal{A} = 1 - \bar{T}_i/\bar{T}_0$ as a function of the fraction of atoms excited to the intermediate state $|e\rangle$, f_e , which is varied using the intensity of the 780 nm ionization laser. The total number of ions N_i in the ionization volume depends linearly on f_e and is given on the top horizontal axis of Fig. 3(c). The relative

absorption first increases steadily with N_i and then saturates rapidly above $N_i \sim 10$. For small N_i where the blockade spheres surrounding the ions are unlikely to intersect, $\mathcal{A} \propto N_i$, as explained in Ref. [27]. When N_i increases, the blockade spheres start to overlap, and the number of scattered photons per ion is reduced, resulting in the saturation of \mathcal{A} . In this regime, the relative absorption reaches $\mathcal{A}_{\text{sat}} \approx 0.4$, which defines the maximum contrast achieved with our current experimental conditions. We infer that a contrast of ~ 0.3 or more can be expected from a single blockade sphere of radius R_b induced by an individual ion.

To obtain a more quantitative understanding of our experimental results, we compare the data of Fig. 3 with the model presented in Refs. [25,27]. The propagation of the probe field \mathcal{E}_P through the atomic cloud is calculated in steady state using the differential equation $\partial_z \mathcal{E}_P(\vec{r}) = i\pi/\lambda_P \chi(\vec{r}) \mathcal{E}_P(\vec{r})$, where $\chi(\vec{r})$ is the linear susceptibility at position \vec{r} . For our effective three-level system, $\chi(\vec{r})$ is approximated as

$$\chi(\vec{r}) = \frac{i n_{\text{at}}(\vec{r}) \Gamma \sigma \lambda_P / 4\pi}{\frac{\Gamma}{2} - i(\Delta_P - \delta_1) + \frac{\Omega_{\text{C,eff}}^2 / 4}{\gamma - i[\Delta_P + \Delta_C - \delta_2 - \delta_{\text{Stark}}(\vec{r})]}}, \quad (2)$$

where $\Gamma/2\pi = 6.067$ MHz is the spontaneous decay rate from state $|e\rangle$, $n_{\text{at}}(\vec{r})$ is the atomic density, γ is a dephasing rate of the atomic coherence between the $|g\rangle$ and $|r_0\rangle$ states, and σ is a scattering cross section. Moreover, Δ_C is the three-photon detuning from the $|e\rangle \rightarrow |r_0\rangle$ atomic transition, and δ_1 and δ_2 are the ac Stark shifts affecting the $|e\rangle$ and $|r_0\rangle$ energy levels, respectively. Finally, $\delta_{\text{Stark}}(\vec{r}) = \alpha(\theta) \mathbf{E}(\vec{r})^2 / 2$ is the Stark shift of $|r_0\rangle$, where $\alpha(\theta)$ is the polarizability depending on θ , the angle between the quantization axis and the direction of the electrostatic field \mathbf{E} at the position \vec{r} [27].

In the simulation, each ion sample is generated given the ionization rate per atom $R_I(\vec{r}) = \rho_{ee}(\vec{r}) \sigma_I \Phi_{479}$, where σ_I is the ionization cross section at the wavelength of the 479 nm laser, Φ_{479} is its photon flux density, and ρ_{ee} is the fractional excitation in the intermediate state $|e\rangle$. The consideration of the ion cloud expansion during the detection pulse, the effect of which may not be negligible for a large ion number, is discussed in Ref. [27]. The simulated curves displayed in Fig. 3 are averages over many ion samples and calculated using $\sigma_I = 20.4$ Mb, which is consistent with the cross section reported in Ref. [33]. With all the other parameters being experimentally calibrated, the good agreement between the data and the simulation confirms that the ion–Rydberg-atom interaction is the sole mechanism responsible for the observed imaging contrast.

Our ion imaging scheme opens up the possibility of spatially investigating ionization processes and the dynamics of ion-atom hybrid systems. We illustrate this in Fig. 4 with a series of images showing the avalanche ionization of

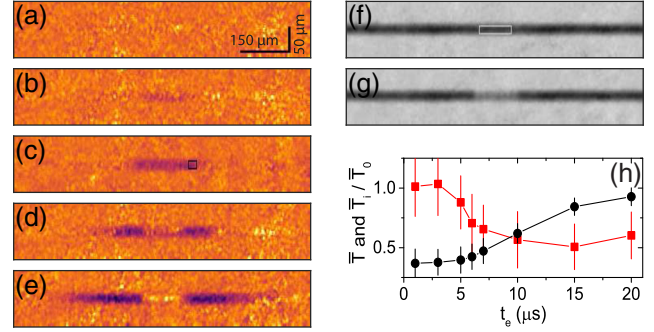


FIG. 4. Avalanche ionization. Interaction induced images of the space charges after an excitation duration $t_e = 0.14 \mu\text{s}$ (a), $3 \mu\text{s}$ (b), $5 \mu\text{s}$ (c), $7 \mu\text{s}$ (d), and $10 \mu\text{s}$ (e). Corresponding absorption images of ground-state atoms acquired after $t_e = 5 \mu\text{s}$ (f) and $10 \mu\text{s}$ (g). (h) Relative transmission (\bar{T}_i/\bar{T}_0) extracted from the ion images at the position just outside the excitation region (red squares) and transmission (\bar{T}) of the absorption images at the center of the excitation region (black dots) vs t_e . The boxes on (c) and (f) indicate the areas for extracting \bar{T}_i/\bar{T}_0 and \bar{T} , respectively.

an atomic gas excited to the $|30D_{5/2}, m_J = 5/2\rangle$ state. For these measurements, the 479 nm ionization laser in Fig. 1 is replaced by a 482 nm laser for the coupling to the Rydberg state, and the excitation is performed with a single slit for a variable duration t_e . After a delay of $0.1 \mu\text{s}$, we either monitor the ion distributions with our imaging scheme in Figs. 1(c) and 1(d) or take absorption images of the ground-state atoms. The images in Fig. 4 are consistent with the well-established avalanche ionization process [34,35], and this is confirmed by the presence of a time threshold in the transmission plots of Fig. 4(h). While no ions are observed at $t_e = 0.14 \mu\text{s}$ [Fig. 4(a)], an initial ionization occurs on the scale of a few microseconds, mostly due to Penning ionization of pairs of cold Rydberg atoms excited to the $|30D_{5/2}, m_J = 5/2\rangle$ state [36]. At this stage, the ion distribution remains localized at the excitation region [Figs. 4(b) and 4(c)], and these few ions barely affect the distribution of the ground-state atoms [Fig. 4(f)]. Once the space charge due to the ions is sufficiently large to trap electrons, the avalanche ionization is set off by electrons colliding with Rydberg atoms and a plasma forms. This process rapidly depletes the ground-state atoms upon continuous coupling the atomic cloud to the Rydberg state [Fig. 4(g)]. With this ion imaging technique, it can be clearly seen in Figs. 4(d) and 4(e) that the plasma expands into the atomic cloud outside the excitation region. We note that the probability of ionizing atoms from state $|r_0\rangle$ during the EIT imaging pulse of $1 \mu\text{s}$ remains small in the presence of the plasma, as Ω_P is low and the fraction of atoms in $|r_0\rangle$ is further suppressed due to the large Stark shifts. Thus, our imaging technique can image the space charge and its expansion with minimum disturbance added to the plasma.

In conclusion, we have demonstrated *in situ* imaging of ions in an atomic ensemble by ion–Rydberg-atom interaction induced absorption, with which we have visualized avalanche ionization processes. One advantage of this imaging technique is that it does not depend on the internal structure of the ionic impurities and can be applied to image a wide range of ion-atom mixtures, including ion species with no cycling optical transitions available. Our technique is currently limited by the low intensity of the probe light, which is used to avoid excess absorption due to Rydberg-Rydberg interactions but prevents us from single-shot imaging. A homodyne detection of the probe light with a reference beam of a 10 times stronger field strength would sufficiently improve the signal-to-noise ratio [37] for spatially resolving individual ions in a single shot.

The authors thank Tom Gallagher and Martin Kiffner for helpful discussions and acknowledge the support by the National Research Foundation, Prime Minister’s Office, Singapore and the Ministry of Education, Singapore under the Research Centres of Excellence Programme.

* wenhui.li@nus.edu.sg

† These two authors contributed equally to this work.

- [1] T. F. Gallagher, *Rydberg Atoms* (Cambridge University Press, Cambridge, England, 1994).
- [2] J. A. Sedlacek, A. Schwettmann, H. Kübler, R. Löw, T. Pfau, and J. P. Shaffer, Microwave electrometry with Rydberg atoms in a vapour cell using bright atomic resonances, *Nat. Phys.* **8**, 819 (2012).
- [3] C. L. Holloway, M. T. Simons, J. A. Gordon, P. F. Wilson, C. M. Cooke, D. A. Anderson, and G. Raithel, Atom-based rf electric field metrology: From self-calibrated measurements to subwavelength and near-field imaging, *IEEE Transactions on Electromagnetic Compatibility* **59**, 717 (2017).
- [4] C. G. Wade, N. Šibalić, N. R. de Melo, J. M. Kondo, C. S. Adams, and K. J. Weatherill, Real-time near-field terahertz imaging with atomic optical fluorescence, *Nat. Photonics* **11**, 40 (2017).
- [5] K. S. Chan, M. Siercke, C. Hufnagel, and R. Dumke, Adsorbate Electric Fields on a Cryogenic Atom Chip, *Phys. Rev. Lett.* **112**, 026101 (2014).
- [6] Y. O. Dudin and A. Kuzmich, Strongly interacting Rydberg excitations of a cold atomic gas, *Science* **336**, 887 (2012).
- [7] T. Peyronel, O. Firstenberg, Q.-Yu Liang, S. Hofferberth, A. V. Gorshkov, T. Pohl, M. D. Lukin, and V. Vuletić, Quantum nonlinear optics with single photons enabled by strongly interacting atoms, *Nature (London)* **488**, 57 (2012).
- [8] H. Busche, P. Huillery, S. W. Ball, T. Ilieva, M. P. A. Jones, and C. S. Adams, Contactless nonlinear optics mediated by long-range Rydberg interactions, *Nat. Phys.* **13**, 655 (2017).
- [9] D. Tiarks, S. Schmidt-Eberle, T. Stolz, G. Rempe, and S. Dürr, A photon-photon quantum gate based on Rydberg interactions, *Nat. Phys.* **15**, 124 (2019).
- [10] M. Saffman, Quantum computing with atomic qubits and Rydberg interactions: Progress and challenges, *J. Phys. B* **49**, 202001 (2016).
- [11] H. Bernien, S. Schwartz, A. Keesling, H. Levine, A. Omran, H. Pichler, S. Choi, A. S. Zibrov, M. Endres, M. Greiner, V. Vuletić, and M. D. Lukin, Probing many-body dynamics on a 51-atom quantum simulator, *Nature (London)* **551**, 579 (2017).
- [12] S. de Léséleuc, V. Lienhard, P. Scholl, D. Barredo, S. Weber, N. Lang, H. P. Büchler, T. Lahaye, and A. Browaeys, Observation of a symmetry-protected topological phase of interacting bosons with Rydberg atoms, *Science* **365**, 775 (2019).
- [13] F. Engel, T. Dieterle, T. Schmid, C. Tomschitz, C. Veit, N. Zuber, R. Löw, T. Pfau, and F. Meinert, Observation of Rydberg Blockade Induced by a Single Ion, *Phys. Rev. Lett.* **121**, 193401 (2018).
- [14] T. Secker, N. Ewald, J. Joger, H. Fürst, T. Feldker, and R. Gerritsma, Trapped Ions in Rydberg-Dressed Atomic Gases, *Phys. Rev. Lett.* **118**, 263201 (2017).
- [15] N. V. Ewald, T. Feldker, H. Hirzler, H. A. Fürst, and R. Gerritsma, Observation of Interaction between Trapped Ions and Ultracold Rydberg Atoms, *Phys. Rev. Lett.* **122**, 253401 (2019).
- [16] A. Härter and J. H. Denschlag, Cold atom-ion experiments in hybrid traps, *Contemp. Phys.* **55**, 33 (2014).
- [17] M. Tomza, K. Jachymski, R. Gerritsma, A. Negretti, T. Calarco, Z. Idziaszek, and P. S. Julienne, Cold hybrid ion-atom systems, *Rev. Mod. Phys.* **91**, 035001 (2019).
- [18] M. D. Lukin, M. Fleischhauer, R. Cote, L. M. Duan, D. Jaksch, J. I. Cirac, and P. Zoller, Dipole Blockade and Quantum Information Processing in Mesoscopic Atomic Ensembles, *Phys. Rev. Lett.* **87**, 037901 (2001).
- [19] T. Vogt, M. Viteau, A. Chotia, J. Zhao, D. Comparat, and P. Pillet, Electric-Field Induced Dipole Blockade with Rydberg Atoms, *Phys. Rev. Lett.* **99**, 073002 (2007).
- [20] G. Günter, M. Robert-de-Saint-Vincent, H. Schempp, C. S. Hofmann, S. Whitlock, and M. Weidemüller, Interaction Enhanced Imaging of Individual Rydberg Atoms in Dense Gases, *Phys. Rev. Lett.* **108**, 013002 (2012).
- [21] G. Günter, H. Schempp, M. Robert-de-Saint-Vincent, V. Gavryusev, S. Helmrich, C. S. Hofmann, S. Whitlock, and M. Weidemüller, Observing the dynamics of dipole-mediated energy transport by interaction-enhanced imaging, *Science* **342**, 954 (2013).
- [22] N. Šibalić, J. D. Pritchard, C. S. Adams, and K. J. Weatherill, ARC: An open-source library for calculating properties of alkali Rydberg atoms, *Comput. Phys. Commun.* **220**, 319 (2017).
- [23] J. D. Pritchard, D. Maxwell, A. Gauguet, K. J. Weatherill, M. P. A. Jones, and C. S. Adams, Cooperative Atom-Light Interaction in a Blocked Rydberg Ensemble, *Phys. Rev. Lett.* **105**, 193603 (2010).
- [24] J. Han, T. Vogt, and W. Li, Spectral shift and dephasing of electromagnetically induced transparency in an interacting Rydberg gas, *Phys. Rev. A* **94**, 043806 (2016).
- [25] T. Vogt, C. Gross, T. F. Gallagher, and W. Li, Microwave-assisted Rydberg electromagnetically induced transparency, *Opt. Lett.* **43**, 1822 (2018).

- [26] J. Han, T. Vogt, M. Manjappa, R. Guo, M. Kiffner, and W. Li, Lensing effect of electromagnetically induced transparency involving a Rydberg state, *Phys. Rev. A* **92**, 063824 (2015).
- [27] See Supplemental Material at <http://link.aps.org/supplemental/10.1103/PhysRevLett.124.053401> for details on the theoretical models and the experimental parameters, which includes Refs. [28–30].
- [28] J. Han, T. Vogt, C. Gross, D. Jaksch, M. Kiffner, and W. Li, Coherent Microwave-to-Optical Conversion via Six-Wave Mixing in Rydberg Atoms, *Phys. Rev. Lett.* **120**, 093201 (2018).
- [29] S. Weber, C. Tresp, H. Menke, A. Urvoy, O. Firstenberg, H. P. Büchler, and S. Hofferberth, Calculation of Rydberg interaction potentials, *J. Phys. B* **50**, 133001 (2017).
- [30] J. Lee, J. Nunkaew, and T. F. Gallagher, Microwave spectroscopy of the cold rubidium $(n+1)d_{5/2} \rightarrow ng$ and nh transitions, *Phys. Rev. A* **94**, 022505 (2016).
- [31] X. Li, M. Ke, B. Yan, and Y. Wang, Reduction of interference fringes in absorption imaging of cold atom cloud using eigenface method, *Chin. Optic. Lett.* **5**, 128 (2007), <https://www.osapublishing.org/col/abstract.cfm?uri=col-5-3-128>.
- [32] M. Fleischhauer, A. Imamoglu, and J. P. Marangos, Electromagnetically induced transparency: Optics in coherent media, *Rev. Mod. Phys.* **77**, 633 (2005).
- [33] A. Nadeem and S. U. Haq, Photoionization from the $5p^2P_{3/2}$ state of rubidium, *Phys. Rev. A* **83**, 063404 (2011).
- [34] M. Robert-de-Saint-Vincent, C. S. Hofmann, H. Schempp, G. Günter, S. Whitlock, and M. Weidemüller, Spontaneous Avalanche Ionization of a Strongly Blockaded Rydberg Gas, *Phys. Rev. Lett.* **110**, 045004 (2013).
- [35] T. M. Weber, T. Niederprüm, T. Manthey, P. Langer, V. Guarrera, G. Barontini, and H. Ott, Continuous coupling of ultracold atoms to an ionic plasma via Rydberg excitation, *Phys. Rev. A* **86**, 020702(R) (2012).
- [36] W. Li, P. J. Tanner, and T. F. Gallagher, Dipole-Dipole Excitation and Ionization in an Ultracold Gas of Rydberg Atoms, *Phys. Rev. Lett.* **94**, 173001 (2005).
- [37] S. Kadlecek, J. Sebby, R. Newell, and T. G. Walker, Nondestructive spatial heterodyne imaging of cold atoms, *Opt. Lett.* **26**, 137 (2001).